Extreme Mechanics Letters 30 (2019) 100501

Contents lists available at ScienceDirect

Extreme Mechanics Letters

journal homepage: www.elsevier.com/locate/eml

Mechanical peeling of van der Waals heterostructures: Theory and simulations

Kui Lin, Ya-Pu Zhao *

State Key Laboratory of Nonlinear Mechanics, Institute of Mechanics, Chinese Academy of Sciences, Beijing 100190, China
School of Engineering Science, University of Chinese Academy of Sciences, Beijing 100049, China

ARTICLE INFO

Article history:
Received 20 March 2019
Received in revised form 13 May 2019
Accepted 14 June 2019
Available online xxxx

Keywords:
van der Waals heterostructures
Mechanical peeling
Density functional theory
Molecular dynamics simulation
Elasto-peeling length

ABSTRACT

Mechanical peeling is crucial for the assembly process of van der Waals (vdW) heterostructures. We provide a new theory to describe the peeling of vdW heterostructures based on interatomic potential. Representatively, we present the peeling of graphene on molybdenum disulfide (MoS_2) using a bottom-up approach. The results show that there are three stages (the initial, stable and jump out of contact stages) in the entire peeling process. We find that the traditional continuum model is only suitable for the stable stage, while our theory can describe the entire process from (the initial unstable) contact to the end of the stable stage. In addition, we discovered a new characteristic length, the elasto-peeling length $L_{ep} = \sqrt{2D/\Delta\gamma} = 4\sigma_0\sqrt{2\pi D/H}$, that is a crucial parameter that reflects the bending (D) and interfacial properties ($\Delta\gamma$) of the layered materials during peeling. Finally, the theory as expressed by the Hamaker constant (H) is presented. Our findings may help to reveal the underlying mechanisms in the peeling of layered materials at the atomic scale.

1. Introduction

The successful peeling of graphene in 2004 [1] has created a new field of atomic-scale materials. Since then, the study of two-dimensional (2D) materials has become an important research topic [2]. 2D materials have unique electronic properties that make it possible to regulate their band gap by changing the number of layers [3–5]. Different 2D materials have different electronic properties. The combination of different 2D materials results in exotic quantum characteristics that enables their broad prospects in future technological applications. Van der Waals (vdW) heterostructures are designed at the atomic scale using layer-by-layer assembly of different 2D materials [6]. The diversity of the electronic structures of vdW heterostructures leads to their functional diversity. The materials enable new functional device designs and have a wide range of applications in the electronics, energy and biomedical fields such as gate-tunable devices [7–9], photodetectors [10,11], light-emitting devices [12–14] and photovoltaic devices [15–17]. However, although vdW heterostructures have promising applications, they are limited by the maturity of their structural assembly technology. Therefore, they have not been widely used at present.

VdW heterostructures are heterogeneous functional materials that are mainly composed of various 2D materials held together by interlayer vdW forces. Numerous kinds of vdW heterostructures can theoretically be assembled. However, the current assembly techniques are limited to the specific interface of 2D materials. It is very challenging to assemble two kinds of materials that have different atomic arrangements and different thermal stabilities. This produces a number of mechanical problems such as surface reconstruction [5,18–20], different thermal stabilities and material strain due to the lattice mismatch [21]. Moreover, the assembly of different 2D materials and the precise control of the interfacial properties are key to obtaining high quality vdW heterostructures. Therefore, the limitations of heterostructure assembly technology seriously hinders the production and use of vdW heterostructures. Currently, the main methods for generating vdW heterostructures include direct growth and mechanical assembly. As a direct growth method, chemical vapor deposition (CVD) has already enabled the growth of many vdW heterostructures [22] such as MoS_2/graphene [23,24] and MoS_2/hBN [25,26]. Furthermore, the most versatile vdW heterostructure assembly technique is direct mechanical assembly [5]. Dean et al. [27] produced high-quality exfoliated mono- and bilayer graphene devices on hexagonal boron nitride (h-BN) substrates by a mechanical transfer process. Coleman et al. [28] and Nicolosi et al. [29] have reported liquid-phase exfoliation, which is a very powerful method for assembling vdW heterostructures and exfoliating 2D materials. Thus, mechanical exfoliation is a key technology in the assembly of heterostructures. Based on continuum methods, Zhang et al. [30] conducted a theoretical study on the peeling mechanics of various 2D materials. Their theory can describe the

* Corresponding author at: State Key Laboratory of Nonlinear Mechanics, Institute of Mechanics, Chinese Academy of Sciences, Beijing 100190, China.
E-mail address: yzhao@imech.ac.cn (Y.-P. Zhao).

https://doi.org/10.1016/j.eml.2019.100501
2352-4316/

peel-off force in the stable state. However, the force in the initial stage is very important for understanding peeling, especially because the peak peeling force appears at this stage. Therefore, it is necessary to develop a new theory based on interatomic potential [31,32] to describe the entire peeling process at the atomic scale.

In this article, we utilize bottom-up methods to investigate the peeling processes of vdW heterostructures. As a typical vdW heterostructure, graphene/MoS_2 is chosen for our simulations. First, the lattice mismatch values, strain energy densities and potential parameters between graphene and MoS_2 are obtained from density functional theory calculations with dispersion corrections (DFT-D2). Second, we investigate the peeling process under vertical force loading and a combination of vertical force and bending moment loadings by using molecular dynamics (MD) simulations, as shown in Fig. 1. The changes in the total energy, elastic energy, vdW interaction potential and peeling force are obtained, and then we compare the peeling forces obtained from these simulation results with those from traditional continuum methods. Third, we conduct a mechanistic analysis of the peeling process and develop a quasi-continuum method to describe the evolution of the peeling force. Finally, we obtain a characteristic length that is a crucial parameter that reflects the bending and interfacial properties of layered materials during peeling. In addition, to generalize the theory, we express it by the Hamaker constant. Our study aims to reveal the underlying mechanisms in the peeling of layered materials at the atomic scale, and we hope that the related mechanisms can provide new insights into the mechanical assembly of vdW heterostructures.

2. Methods

2.1. Density functional theory

The optimized structures of graphene and MoS_2 were calculated by density functional theory (DFT) within the Vienna *Ab initio* Simulation Package (VASP) [33,34]. The projected augmented wave (PAW) method was used to describe the interactions between the valence electrons and the ionic core. We used the generalized gradient approximation (GGA) with exchange and correlation functionals, according to the approach proposed by Perdew, Burke and Ernzerhof (PBE). The electronic wave functions were expended in a plane-wave basis with a cut off at 400 eV, which was high enough to ensure no Pulay stress occurred during relaxation. The convergence criteria of the energy and force for structural relaxation were set to 10^{-5} eV and 0.01 eV $Å^{-1}$, respectively. The Brillouin zone was sampled by using the Monkhorst–Pack methodology with a $5 \times 5 \times 1$ area for the geometry optimization and binding energy calculations. To calculate the binding energy between graphene and MoS_2, we chose the vdW correction proposed by Grimme (DFT-D2) [35,36] due to its good description of long-range vdW interactions. In the calculations, a 5×5 primitive cells of graphene and a 4×4 primitive cells of MoS_2 as a typical supercell of MoS_2/graphene heterostructures [37] were used to calculate their respective optimized lattice parameters. After optimizing the structures of graphene and MoS_2, we fixed MoS_2 as the substrate and moved graphene at different distances to calculate the interlayer binding energy. The vacuum space in the direction perpendicular to the surface was approximately 20 Å to separate neighboring slabs.

2.2. Molecular dynamics simulations

Large-scale molecular dynamics (MD) simulations were carried out using LAMMPS to explore the peeling processes [38]. We simulated the peeling process of graphene on MoS_2 under two kinds of loading conditions, and the models are shown in Fig. 1. In the x and z directions, we used nonperiodic and fixed boundary conditions, and a periodic boundary was applied in the y direction. The interaction potential parameters between graphene and MoS_2 were obtained based on our *Ab initio* calculations. MoS_2 was treated as a virtual wall. We employed a 12-6 Lennard-Jones (LJ) potential to simulate the weak vdW interaction between the C atom and the MoS_2 wall. The adaptive intermolecular reactive empirical bond order (AIREBO) potential [39], which has been widely adopted to investigate the mechanical properties of graphene [40,41], was used to model the interactions of the C-C atoms in graphene. All interactions were calculated with a cutoff of 12 Å. The MD simulations were performed in an NVT ensemble (constant number of atoms, volume and temperature) while using the Nose–Hoover method to regulate the temperature at 0.1 K, and the time step was 1 fs. To simulate the two kinds of peeling processes, we moved and then fixed either the first or the first two column atoms on the tip of graphene at 0.05 Å each time. Then, 10 ps simulations were performed each time to optimize the structure.

3. Results and discussion

3.1. Lattice mismatches and the interaction potential between graphene and MoS_2

Through DFT calculations, see Fig. 2(a) and (b), we obtained the optimized supercells of graphene and MoS_2. The optimized lattice parameters of graphene and MoS_2 are 2.466 Å and 3.183 Å, respectively. After considering the vdW interactions between graphene and MoS_2, the DFT-D2 calculation is performed, and the final optimized lattice parameters of graphene and MoS_2 are 2.489 Å and 3.113 Å, respectively, as shown in Fig. 2(c). Therefore, when graphene is combined with MoS_2, it results in a lattice mismatch that is defined as:

$$\varepsilon_{\mathrm{m}} = \left(a_{\mathrm{combine}} - a_{\mathrm{sin\,gle}}\right)/a_{\mathrm{sin\,gle}}, \tag{1}$$

where $a_{\mathrm{sin\,gle}}$ and a_{combine} are the lattice constants of the single material and combined material, respectively. Graphene is elongated with a 0.93% lattice mismatch, and MoS_2 is compressed with a −2.20% lattice mismatch. Additionally, the intrinsic strain energy density E_{sed} that is caused by the lattice mismatch can be calculated by:

$$E_{\mathrm{sed}} = \left(E_{\mathrm{Graphene/MoS_2}} - E_{\mathrm{single}}\right)/A, \tag{2}$$

with the potential of graphene or MoS_2 in the heterostructure represented by $E_{\mathrm{Graphene/MoS_2}}$, that of single graphene or MoS_2 by E_{single}, and A represents the area of the heterostructure. The intrinsic strain energy densities of graphene and MoS_2 in the heterostructure are 1.8404 meV/$Å^2$ and 15.5131 meV/$Å^2$, respectively. The binding energy is given according to:

$$E_{\mathrm{b}} = -\left(E_{\mathrm{Graphene@MoS_2}} - E_{\mathrm{Graphene}} - E_{\mathrm{MoS_2}}\right), \tag{3}$$

where E_{Graphene}, $E_{\mathrm{MoS_2}}$ and $E_{\mathrm{Graphene@MoS_2}}$ are the total energies of graphene, MoS_2 and the graphene/MoS_2 heterostructure, respectively. The lattice mismatch values, strain energy densities and related parameters are presented in Table 1, and other unique parameters are given in Supplementary Table S1. In particular, due to the accuracy of MD simulation, the influence of intrinsic strain energy is neglected in subsequent MD simulations. The effect of intrinsic strain energy is only reflected in the potential parameters used in our MD simulations.

For the homogeneous deformation caused by the lattice mismatch, we can use the Cauchy-Born rule to extrapolate information from the atomic scale to the microscale [42]. As shown in Fig. 2(e), $\varphi(\boldsymbol{X}, t)$ can denote the deformation function, which

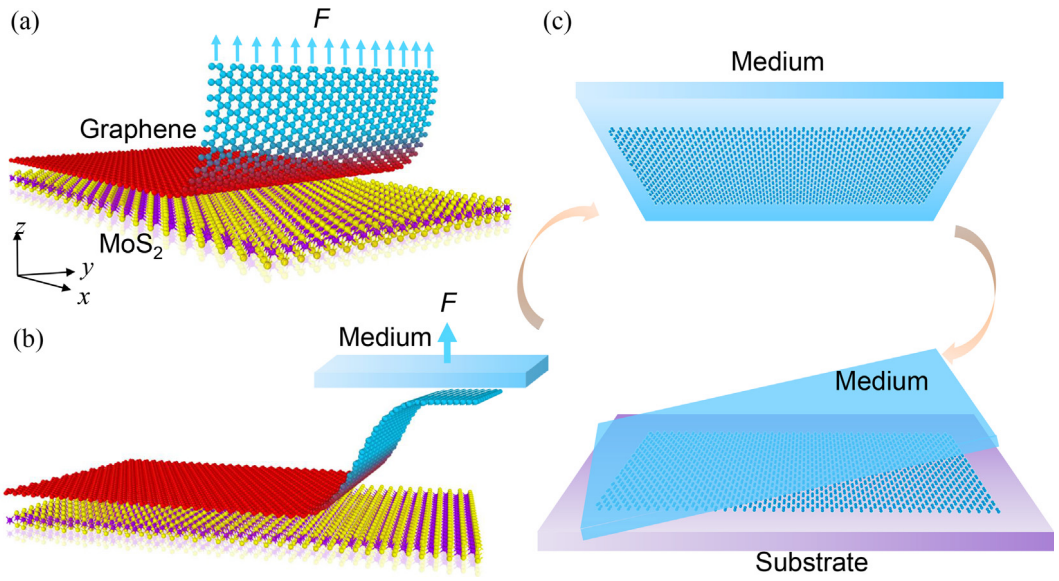

Fig. 1. Simulation models for peeling: The top layer is graphene while the bottom layer is MoS_2. The red region indicates the atoms that are subjected to the action of the vdW force from the bottom. (a) Peeling model under vertical force loading. (b) Peeling model under vertical force and bending moment loadings, which are caused by the adhesion of the medium. (c) Transfer of a 2D material from one substrate to another.

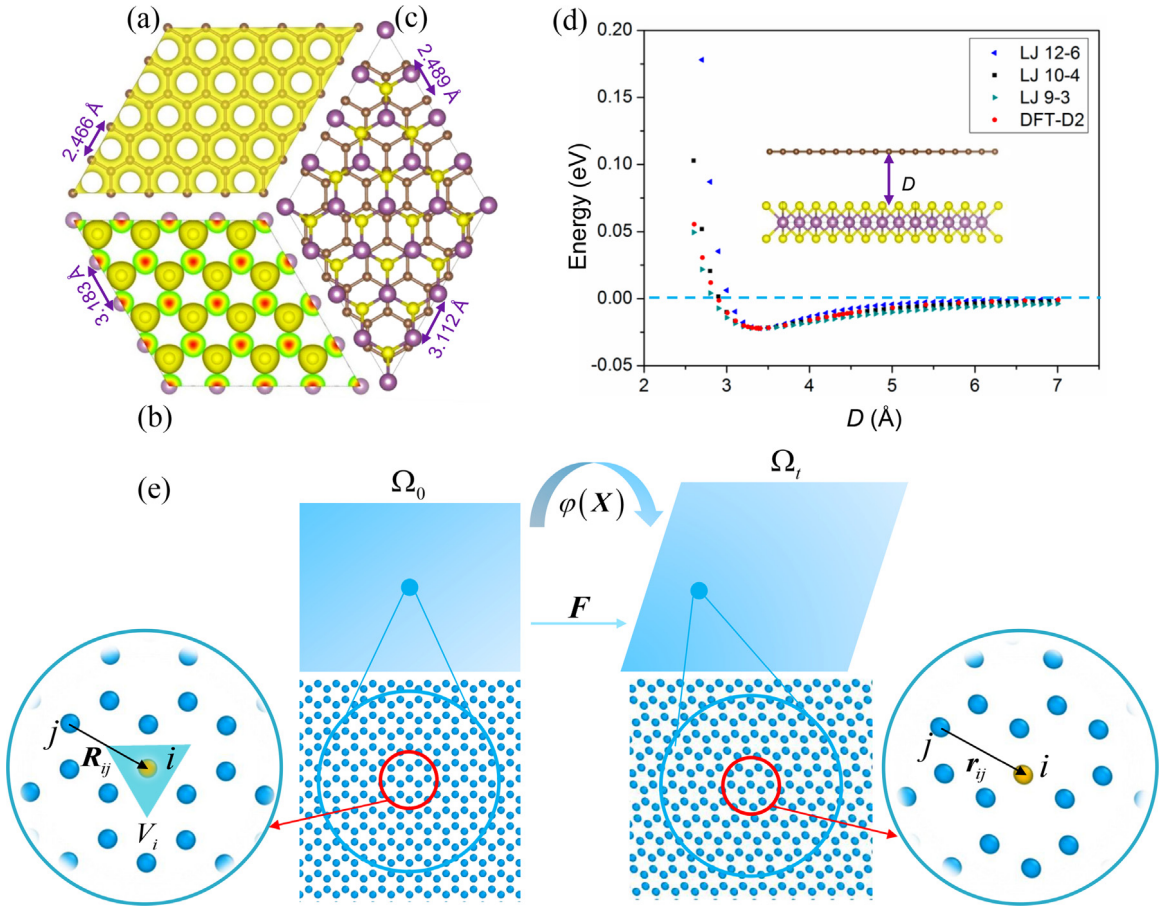

Fig. 2. (a) Optimized electronic structure and lattice constant (3.466 Å) of graphene. (b) Optimized electronic structure and lattice constant (3.183 Å) of MoS_2. (c) Lattice mismatch of graphene on MoS_2. The lattice constant of graphene is elongated to 2.489 Å, and that of MoS_2 is shortened to 3.112 Å. (d) Red indicates the binding energy between a C atom and the monolayer of MoS_2 as calculated by the DFT-D2 method. Blue, black and dark cyan are the fitting results for the LJ 12-6, LJ 10-4 and LJ 9-3 potentials, respectively. The insert is a side view of monolayer graphene and MoS_2 with spacing D. (e) Cauchy–Born rule for the case of the homogeneous deformation of graphene.

relates the points $\boldsymbol{X}$ in a reference configuration Ω_0 (the equilibrium configuration of each single layer) to the points $\boldsymbol{x} = \varphi(\boldsymbol{X}, t)$ in the current configuration Ω_t (the equilibrium configuration of each layer in heterostructure). The two-point tensor $\boldsymbol{F}$ is thus

Table 1
Lattice mismatch values, strain energy densities and related parameters for the Graphene/MoS_2 vdW heterostructure.

	Graphene	MoS_2	Graphene@MoS_2	
	(5 × 5)	(4 × 4)	Graphene	MoS_2
Lattice constant a (Å)	2.466	3.183	2.489	3.113
ε_m	–	–	0.93%	−2.20%
E_{sed} (meV/Å^2)	–	–	1.8404	15.5131
Binding energy E_b (eV)	–	–	−1.1045	

defined as:

$$\boldsymbol{F} = \frac{\partial \varphi(\boldsymbol{X})}{\partial \boldsymbol{X}} = \frac{\partial x_i}{\partial X_A} e_i \otimes e_A \quad (i = 1, 2, 3; A = \mathrm{I}, \mathrm{II}, \mathrm{III}), \tag{4}$$

where $\boldsymbol{e}_i$ and $\boldsymbol{e}_A$ are the bases of the current configuration and reference configuration, respectively. Therefore, the related atomic distance $\boldsymbol{r}_{ij}$ in the current configuration Ω_t can be obtained from the corresponding relative atomic distance $\boldsymbol{R}_{ij}$ in the reference configuration by the deformation gradient $\boldsymbol{F} = \mathbf{I} + \boldsymbol{H}$. Hence, the Cauchy-Born rule is defined as:

$$\boldsymbol{r}_{ij} = \boldsymbol{F} \cdot \boldsymbol{R}_{ij} = (\mathbf{I} + \boldsymbol{H}) \cdot \boldsymbol{R}_{ij}, \tag{5}$$

where $\mathbf{I}$ is the 2 × 2 identity matrix, and $\boldsymbol{H}$ is the displacement gradient tensor. For homogeneous deformations, the symmetric displacement gradient is identical to the Cauchy strain tensor $\boldsymbol{\varepsilon}$ such that:

$$\boldsymbol{\varepsilon} \equiv \frac{1}{2}\left(\boldsymbol{H} + \boldsymbol{H}^T\right) = \boldsymbol{H} = \frac{\partial \varphi(\boldsymbol{X})}{\partial \boldsymbol{X}} - \mathbf{I}. \tag{6}$$

No shear deformation occurs under a lattice mismatch in this case, hence $\gamma = 0$ and we obtain:

$$\begin{pmatrix} \varepsilon_1 \\ \varepsilon_2 \end{pmatrix} = \begin{pmatrix} \dfrac{\partial \varphi(X_1)}{\partial X_1} - 1 \\ \dfrac{\partial \varphi(X_2)}{\partial X_2} - 1 \end{pmatrix}. \tag{7}$$

Then, the Cauchy strain tensor for graphene $\boldsymbol{\varepsilon}^\alpha$ and MoS_2 $\boldsymbol{\varepsilon}^\beta$ in the vdW heterostructures are:

$$\boldsymbol{\varepsilon}^\alpha = \begin{pmatrix} 0.00930 & \\ 0 & 0.0093 \end{pmatrix} \text{ and } \boldsymbol{\varepsilon}^\beta = \begin{pmatrix} -0.0220 & 0 \\ 0 & -0.0220 \end{pmatrix}. \tag{8}$$

In our calculations, the optimal distance between a monolayer of MoS_2(S atom) and graphene is 3.31 ± 0.02 Å, and the binding energy is −22.1 meV per C atom. These two parameters are very close to the values of the first principles predictions at approximately 3.32 Å and −23 meV in Ref. [43], or 3.30 Å and −23 meV in Ref. [44]. The changes in the binding energy (per C atom) between graphene and MoS_2 are shown in Fig. 2(d). LJ 12-6, LJ 10-4 and LJ 9-3 potentials are used to fit the changes in binding energy. For the LJ 12-6 potential, the energy is given as:

$$E_{12-6}(r) = 4\varepsilon\left[\left(\frac{\sigma_1}{r}\right)^{12} - \left(\frac{\sigma_1}{r}\right)^{6}\right]. \tag{9}$$

The energy and distance parameters are $\varepsilon = 22.1$ meV and $\sigma_1 = 2.96$ Å. For the LJ 10-4 potential, the energy is given by (see Supplementary Note 1 for details):

$$E_{10-4}(r) = \varepsilon_2\left[\frac{1}{10}\left(\frac{\sigma_2}{r}\right)^{10} - \frac{1}{4}\left(\frac{\sigma_2}{r}\right)^{4}\right]. \tag{10}$$

The energy and distance parameters are $\varepsilon_2 = 147.3$ meV and $\sigma_2 = 3.33$ Å. For the LJ 9-3 potential, the energy is given by (see Supplementary Note 2 for details):

$$E_{9-3}(r) = \varepsilon_3\left[\frac{2}{15}\left(\frac{\sigma_3}{r}\right)^{9} - \left(\frac{\sigma_3}{r}\right)^{3}\right]. \tag{11}$$

The energy and distance parameters in the LJ 9-3 potential are $\varepsilon_3 = 21$ meV and $\sigma_3 = 3.86$ Å, respectively.

The LJ 10-4 potential is used to describe the potential of the interactions between particles and planes (single-layers of atoms); the LJ 9-3 potential is used to describe the interactions between particles and semicontinuous space. In this case, MoS_2 or other heterostructure materials are multilayered atomic structures with a certain thickness. As shown in Fig. 2(d), it is clear that the LJ 9-3 and LJ 10-4 potentials can better describe the phase repulsion when the distance is less than the equilibrium distance, while all three potential functions can describe the attraction when the distance is larger than the equilibrium distance. However, the peeling process is a process of resisting substrate attraction. Therefore, we can choose any of them to describe the process. The subsequent calculations and analyses are based on the LJ 12-6 potential.

3.2. MD simulations of peeling under vertical force loading

Vertical peeling is a classical peeling model. The macroscopic continuum mechanics model of vertical peeling was established based on the changes in the interfacial energy during peeling processes. To investigate microscopic peeling on the atomic scale, we simulated two different sizes of graphene exfoliation from MoS_2: a1 × b1 (5.04 nm × 2.91 nm) and a2 × b2 (10.21 nm × 5.89 nm). We simulate a quasi-static peeling process by moving the first column atoms of the boundary 0.05 Å in the vertical direction each step and then fixing the height prior to relaxation, as shown in Fig. 3(a). In peeling processes, total potential energy is composed of:

$$\phi = \frac{1}{2}\iiint_{V_{\text{film}}} \boldsymbol{\sigma}^\alpha : \boldsymbol{\varepsilon}^\alpha \mathrm{d}V + \frac{1}{2}\iiint_{V_{\text{substrate}}} \boldsymbol{\sigma}^\beta : \boldsymbol{\varepsilon}^\beta \mathrm{d}V + \iiint_{V_{\text{film}}} E\left(\left|\boldsymbol{r}^{\alpha\beta}\right|\right) \mathrm{d}V - \boldsymbol{F} \cdot \boldsymbol{u}. \tag{12}$$

The right-hand side is, sequentially, the strain energy of the film (not limited to graphene), the strain energy of the substrate, the vdW interaction energy between the film and substrate and the potential of the external force. The total increase of the first three terms is equal to the increase of the total energy of the simulation. The total energy is given by:

$$E_{\text{total}} = \underbrace{\left\langle \sum_{i,j\neq i}^{M} E\left(r_{i,j}^{\alpha}\right)\right\rangle + \left\langle \sum_{i,j\neq i}^{N} E\left(r_{i,j}^{\beta}\right)\right\rangle}_{E_{\text{def}}} + \underbrace{\left\langle \sum_{i}^{M}\sum_{j}^{N} E\left(r_{i,j}^{\alpha\beta}\right)\right\rangle}_{E_{\text{vdW}}}, \tag{13}$$

where E_{vdW} is the interaction potential between graphene and MoS_2, and E_{def} is the deformation energy of graphene and MoS_2. In this simulation, the deformation energy of the substrate is treated as a constant. Considering the evolution of the peeling configuration over the entire process, we can divide peeling into three stages: the initial stage (I), stable stage (II) and jump out of contact stage (III), as shown in Fig. 3(a). In stage I, the bending deformation of graphene increased as the peeling process progressed. Then, the configuration of the curved portion of graphene remains essentially constant during stage II, which is the stable peeling stage. Finally, the graphene begins to jump out of contact with MoS_2 and returns to the vertical state under action of the bending potential energy of graphene. The variations of each energy component are illustrated in Fig. 3(b) and (c). In Fig. 3(b), we can see that the vdW interaction energy between graphene and MoS_2 is nearly equal to the total energy, and the difference between the two energies is the elastic energy of graphene, as shown in Fig. 3(c). Obviously, the energies are proportional to the size of the material. According to the variations in the elastic

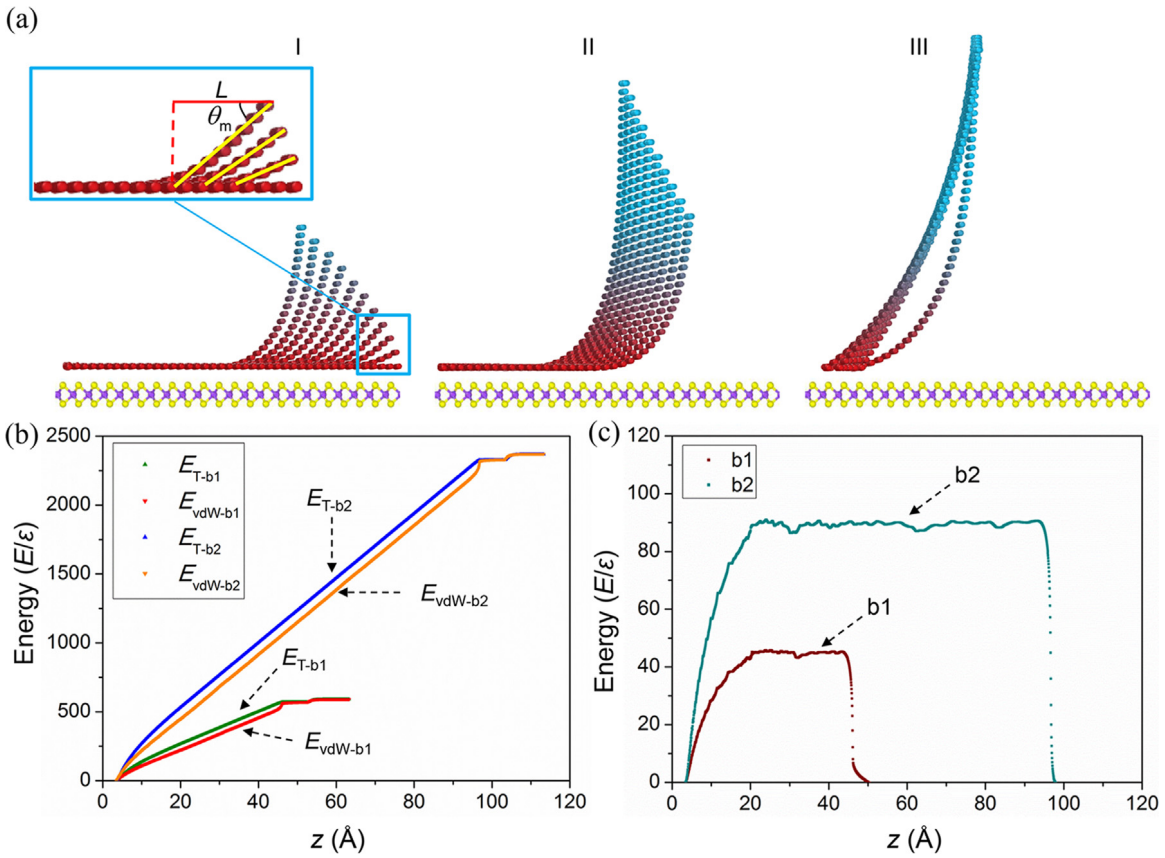

Fig. 3. Vertical peeling of graphene from MoS_2. (a) Three stages of the peeling process: (I) initial stage, (II) stable stage and (III) jump out of contact stage. (b) Evolutions of the dimensionless total energy (green and blue) and vdW interaction energy (red and orange) between graphene and MoS_2 calculated for two sizes: a1 × b1 (5.04 nm × 2.91 nm) and a2 × b2 (10.21 nm × 5.89 nm). (c) Evolution of the dimensionless elastic energy of graphene for the two sizes: a1 × b1 (dark red) and a2 × b2 (dark cyan).

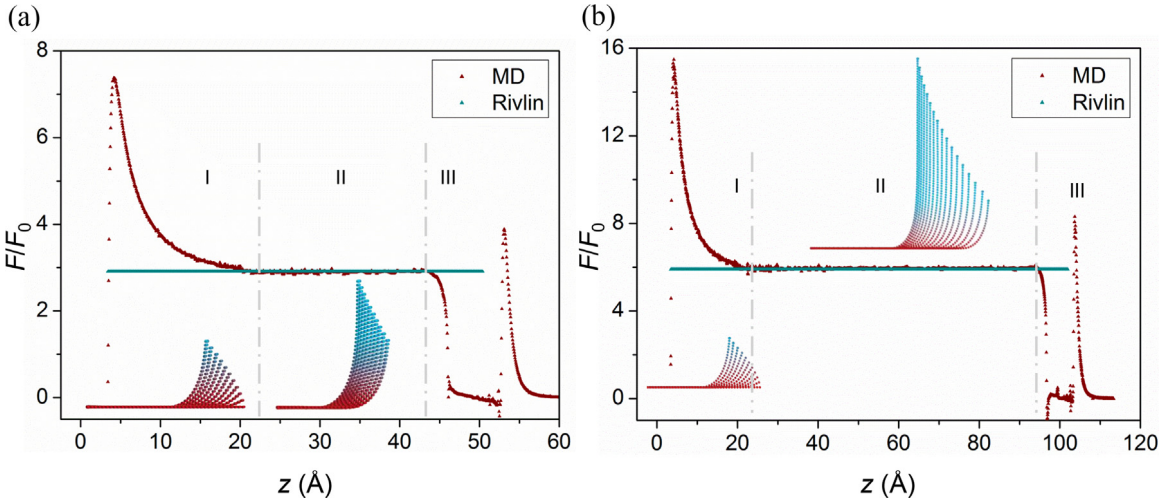

Fig. 4. The evolution of the dimensionless force, red and blue are the MD simulation results and Rivlin model results, respectively, for (a) a width of b1 = 2.91 nm and (b) a width of b1 = 5.89 nm. The inserts are the configurations of the corresponding stage.

energy, we can see that it is divided into three phases: the bending energy increase phase, invariant phase and release phase of graphene, which correspond to the three peeling stages. All the energies are expressed by the dimensionless energy E/ε, where ε is the binding energy between a C atom and MoS_2.

By calculating the gradient of the total energy in the vertical peeling direction z, we can obtain the external force on all the atoms, which is the peeling force (a conservative force) and is defined as:

$$\boldsymbol{F} = -\nabla E_{\text{total}}(\boldsymbol{z}). \tag{14}$$

In addition, vertical peeling, as a classical peeling model, can be described by the continuum mechanics model, which was established by Rivlin [45] and Kendall [46]:

$$F = \Delta\gamma b. \tag{15}$$

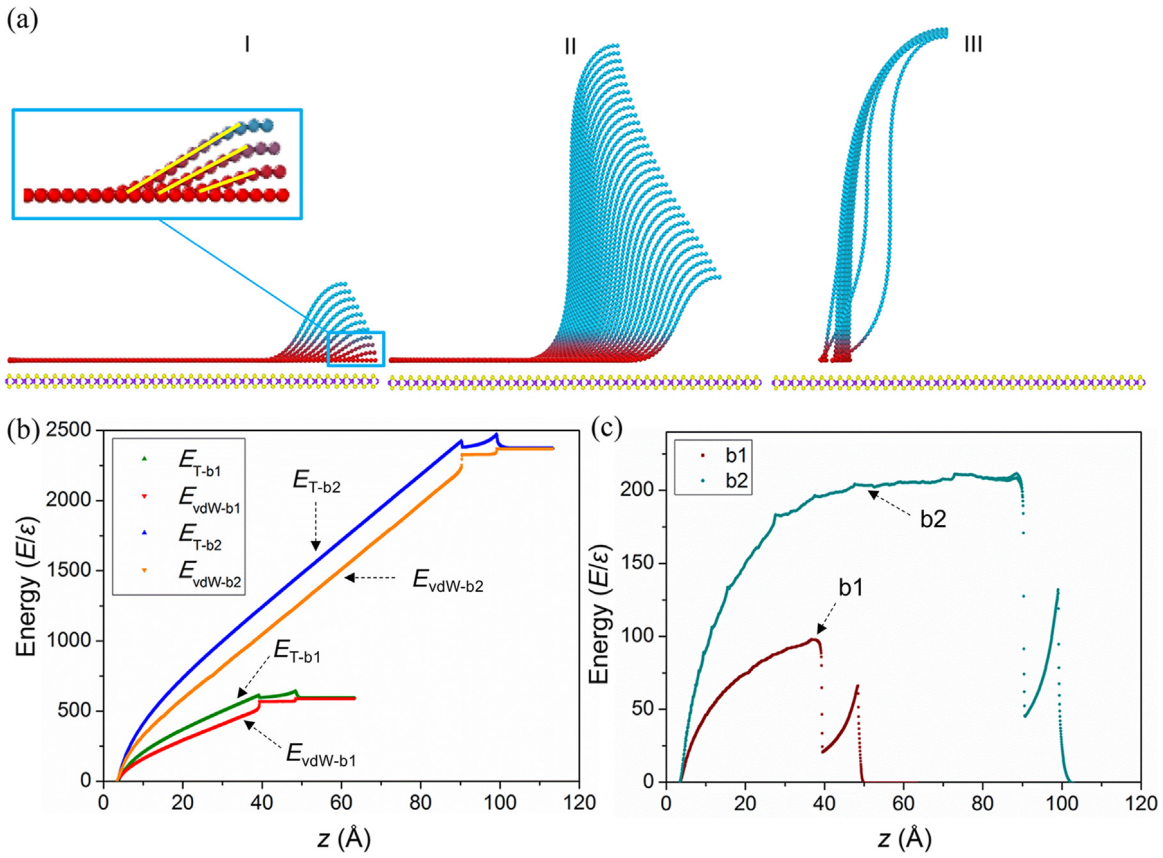

Fig. 5. Peeling of graphene from MoS_2 under the combined action of vertical force and bending moment loadings. (a) Evolution of the configurations in the three stages of the peeling process: (I) initial stage, (II) stable stage and (III) jump out of contact stage. (b) Evolutions of the dimensionless total energy (green and blue) and vdW interaction energy (red and orange) between graphene and MoS_2 for two sizes: a1 × b1 and a2 × b2. (c) Evolution of the dimensionless elastic energy of graphene for two sizes: a1 × b1 (dark red) and a2 × b2 (dark cyan)

where $\Delta\gamma$ is the work of adhesion and b is the interface width. Here, the work of adhesion is the product of the binding energy per C atom ε and the atomic number density ρ. Hence, Eq. (15) becomes:

$$F = \varepsilon\rho b. \tag{16}$$

The force required to peel a 1 nm wide material is $F_0 = \varepsilon\rho$. Therefore, the dimensionless force F/F_0 obtained by the MD simulations and the Rivlin model are presented in Fig. 4. According to the MD simulation results, there is a peak force in the initial stage, and the Rivlin model can only describe the stable peeling stage. When the edge of the graphene begins to jump out of contact with MoS_2, the force will change dramatically due to the release of the elastic energy of graphene. In addition, from Fig. 3(c) and Fig. 4(a) and (b), it can be seen that the peeling height in stage I ($\Delta h = z - z_0 \approx 2$ nm) is independent from the size of the graphene. The height is related to the interfacial properties (work of adhesion) and mechanical properties (bending rigidity) of the material which will be discussed in the following chapters.

3.3. MD simulations for peeling by adhesion

In practice, a vertical force acting directly on the tip of a thin film at the atomic scale is very unlikely. Instead, we may be able to use another medium that has a stronger adhesion to the film to exfoliate the film from the original substrate. In this case, one end of the film is under the action of adhesion, which is equivalent to the effects of the vertical force and bending moment of the medium. Hence, we consider the peeling of graphene from MoS_2 in this loading situation. Fig. 5(a) shows the three stages of the peeling process, which are similar to those of the vertical peeling process mentioned in the previous section. The difference is that both ends of the peeled graphene are in a curved state. Obviously, the total elastic energy will be composed of the bending elastic energy of the two ends. Variations in the various energy components are illustrated in Fig. 5(b) and (c). The difference between the total energy and the vdW interaction energy is larger than that of the case discussed in the previous section because the two ends of the peeled graphene are in a curved state. Moreover, the energies are still proportional to the peeling width b.

Although the end of the film is subjected to the action of the vertical force and bending moment, the work of bending moment loading is zero due to the rotation angle being zero throughout the entire process. Hence, by calculating the gradient of the total energy, we can directly obtain the force on all the atoms. Then, the dimensionless force F/F_0 obtained by the MD simulations and the Rivlin model are presented in Fig. 6. Under this loading condition, a larger force is required in the initial delamination stage, and a longer peeling distance is needed for this stage to reach completion. As shown in Fig. 6(a), due to the graphene being too short, the peeling is completed during the initial stage; hence, there is no stable peeling stage. When the peeling height is greater than a certain value ($\Delta h \approx 4$ nm), a stable stage occurs. Similarly, in the stable stage, the configuration of both ends of the peeled graphene no longer changes. Hence, the force is stable and equal to the force needed for the adhesion work, as shown in Fig. 6(b).

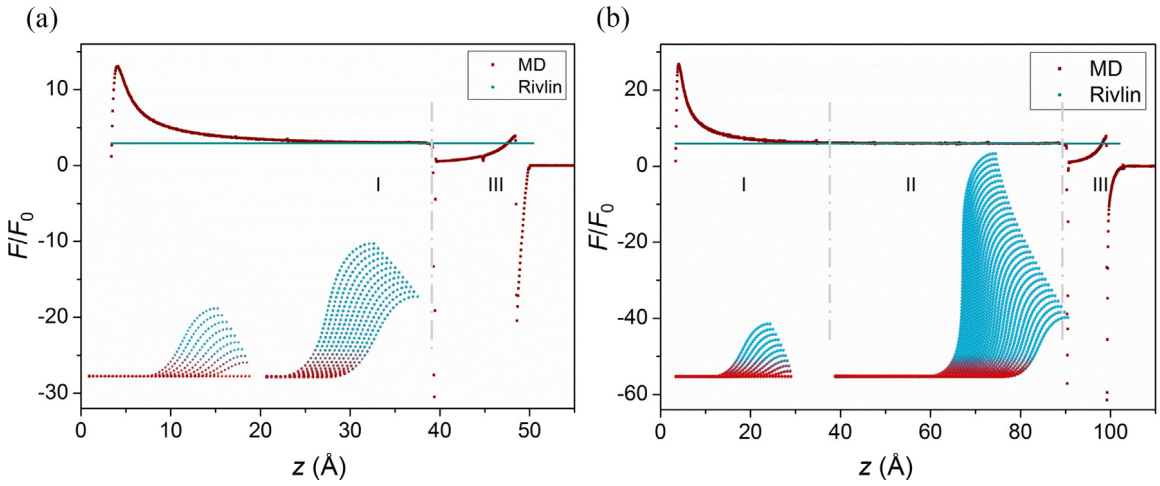

Fig. 6. The evolution of the dimensionless force, red and blue are the MD simulation results and the Rivlin model results, respectively, for (a) a width of b1 = 2.91 nm and (b) a width of b2 = 5.89 nm. The inserts are the configurations of the corresponding stage.

3.4. Mechanical analysis of the peeling process

From the results of the previous sections, we find that traditional method (Rivlin model) can only describe the stable peeling stage. At the initial stage of peeling, the vdW force will gradually increase from zero to the peak and then decrease until the configuration is constant. Moreover, the peak force during the initial stage whose force is several times greater than the stable peeling force. Hence, we cannot ignore an accurate description of this stage, and we need to explore a new theory to describe the peeling process at the atomic scale. Peeling is a moving boundary problem with large deformation. Because our investigation is a quasi-static peeling process, the force state of the film can be carried out via static analysis.

The mechanical models of the two loading methods are shown in Fig. 7, and Fig. 7(a) and (d) represent the peeling of graphene under the two loading conditions. The yellow and red represent no force and the attractive force from the substrate, respectively. Moreover, between these two regions, there is an extremely small area with a width of $d_0 \approx 0.6$ nm in which the atoms experience a repulsive force. The local force states are shown in Fig. 7(b) and (e). Blue indicates the distribution of the repulsive force, and red is the distribution of the attractive force. Generally, based on the Saint-Venant principle, the distributed forces are equivalent to the bending moment and force, as shown in Fig. 7(c) and (f).

In the peeling process, the vdW forces are mainly concentrated in the peeled area near the contact line. Hence, we can treat the quasi-static peeling of graphene as a curved cantilever film. When the peeling distance reaches z, the equilibrium condition of the system is:

$$\mathrm{d}\left(E_{\mathrm{vdW}} + E_{\mathrm{def}} - Fz\right)/\mathrm{d}z = 0, \tag{17}$$

From Fig. 3(b), we can see that the elastic deformation energy (including the bending deformation energy and the elongation deformation energy) is one order of magnitude smaller than the van der Waals interaction energy. In addition, the relationship between the various energies and the position of the peak force at the initial stage are more clearly shown in Fig. 8. It can be seen that the vdW interaction energy accounts for the vast majority of the total energy, which is the key to the peak force. Therefore, the deformation energy is neglected in our theoretical analysis. The peeling force and vdW force are the balance force during the quasi-static peeling process. Hence, we have:

$$F = F_{\mathrm{vdW}} = b\rho \int_{z_0}^{z} \frac{E'(r)}{\sin\theta(r)}\mathrm{d}r. \tag{18}$$

where $E(r)$ is the van der Waals potential energy mentioned in Eqs. (9), (10) and (11); here we choose the LJ 12-6 potential which is used in MD simulations. $\theta(r)$ is the angle between the tangent of the film (graphene) and the positive direction of the x-axis. We approximate $\theta(r)$ as $\theta_{\mathrm{m}}(z)$, which is the tangential angle at the middle of the peeled section. It is a function of the tip height z, hence, $\sin\theta_{\mathrm{m}}(z)$ can be regarded as independent within Eq. (18). Notably, it is very close to the real configuration of the initial stage (the beginning of stage I) in our simulations, as shown in Fig. 3(a) I. Hence, from Eq. (18) we can obtain the value of peeling force:

$$F = b\rho \int_{z_0}^{z} \frac{E'(r)}{\sin\theta_{\mathrm{m}}}\mathrm{d}r = \frac{b\rho\varepsilon}{\sin\theta_{\mathrm{m}}}\left\{4\left[\left(\frac{\sigma_1}{z}\right)^{12} - \left(\frac{\sigma_1}{z}\right)^{6}\right] + 1\right\}. \tag{19}$$

Next, we just need to determine the expression of $\sin\theta_{\mathrm{m}}$. Considering that film peeling corresponds to large deformation bending, the differential equation of the deflection curve is:

$$\frac{\frac{\mathrm{d}^2 z}{\mathrm{d}x^2}}{\left[1 + \left(\frac{\mathrm{d}z}{\mathrm{d}x}\right)^2\right]^{3/2}} = \frac{M(x)}{Db}, \tag{20}$$

where $M(x)$ is the moment equation and D is the bending rigidity. Substituting $\mathrm{d}z/\mathrm{d}x = \tan\theta$ into Eq. (20), we have:

$$\frac{\mathrm{d}\tan\theta}{\left(1 + \tan^2\theta\right)^{3/2}} = \frac{M(x)}{Db}\mathrm{d}x, \tag{21}$$

and then:

$$\frac{\tan\theta}{\left(1 + \tan^2\theta\right)^{1/2}} = \int_0^x \frac{M(x)}{Db}\mathrm{d}x. \tag{22}$$

In the case of concentrated loads at both ends, the moment equation is $M(x) = F(L - x)$, where L is the projected length of the peeled section. Thus, Eq. (22) becomes:

$$\sin\theta = \frac{F}{Db}\left(Lx - \frac{x^2}{2}\right). \tag{23}$$

When $x = L/2$, we have:

$$\sin\theta_{\mathrm{m}} = \frac{3FL^2}{8Db}. \tag{24}$$

Combining Eqs. (19) and (24), we can obtain:

$$\sin^2\theta_{\mathrm{m}} = \frac{3\rho\varepsilon L^2}{8D}\left\{4\left[\left(\frac{\sigma_1}{z}\right)^{12} - \left(\frac{\sigma_1}{z}\right)^{6}\right] + 1\right\}. \tag{25}$$

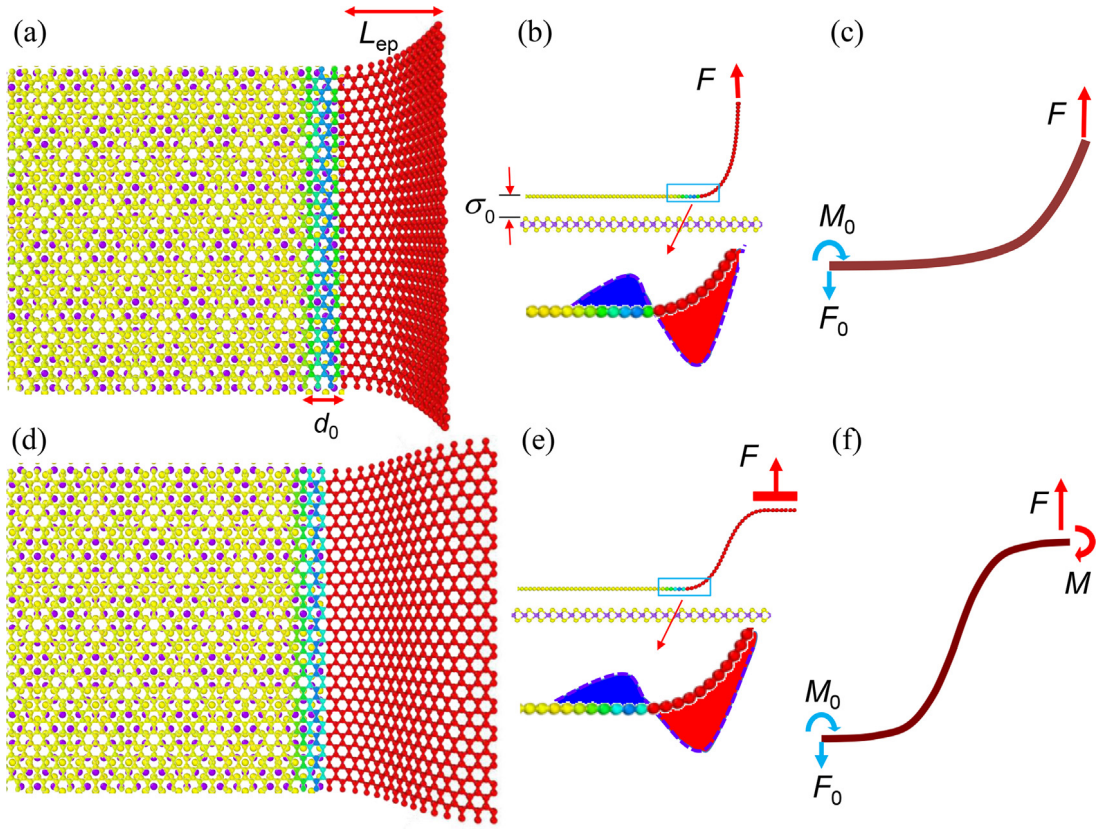

Fig. 7. Mechanical models of the peeling under two different loadings. (a), (b) and (c) correspond to peeling under vertical force loading. (d), (e) and (f) correspond to peeling under vertical force and bending moment loadings. (a) and (d) show the perspective of graphene during peeling; yellow and red regions represent the atoms in the equilibrium position and attraction region, respectively; the middle regions of width d_0 represent the atoms in the repulsive region. (b) and (e) show the side view and force distribution of graphene, for which blue is the respective force and red is the attractive force. (c) and (f) are simplified mechanical models of peeling. (For interpretation of the references to colour in this figure legend, the reader is referred to the web version of this article.)

At the beginning of stage I, especially from the beginning of peeling to the peak force, the peeling height ($\Delta h \sim 1$ Å) and the bond length between atoms (1.42 Å) have the same order of magnitude. Hence, the degree of bending of the graphene is very small, as shown in Fig. 3(a) I. It can then be assumed that the expression of L is

$$L = \frac{(z-\sigma_0)}{\tan\theta_m}, \tag{26}$$

where σ_0 is the equilibrium position. Combining Eqs. (25) and (26), we obtain:

$$\frac{\tan^4\theta_m}{1+\tan^2\theta_m} = \frac{3\rho\varepsilon}{2D}\left\{\left[\left(\frac{\sigma_1}{z}\right)^{12}-\left(\frac{\sigma_1}{z}\right)^{6}\right]+0.25\right\}\left(z-\sqrt[6]{2}\sigma_1\right)^2. \tag{27}$$

Solving Eq. (27) by Taylor expansion at the equilibrium position $\sigma_0 = \sqrt[6]{2}\sigma_1$, we obtain:

$$\tan\theta_m = \frac{\sqrt{3}}{2^{1/3}}\left(\frac{3\rho\varepsilon}{D\sigma_1^2}\right)^{1/4}\left(z-\sqrt[6]{2}\sigma_1\right) - \frac{7\times\sqrt{3}}{4\sqrt{2}\sigma_1}\left(\frac{3\rho\varepsilon}{D\sigma_1^2}\right)^{1/4}\left(z-\sqrt[6]{2}\sigma_1\right)^2 + o[z-\sqrt[6]{2}\sigma_1]^3. \tag{28}$$

By linearly approximating the function near the equilibrium position, this becomes:

$$\tan\theta_m \approx \sqrt{3}\left(\frac{\rho\varepsilon}{2D\sigma_0^2}\right)^{1/4}(z-\sigma_0)$$

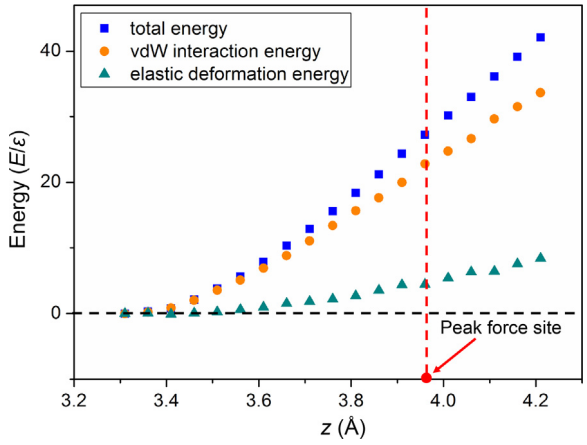

Fig. 8. Evolutions of the dimensionless total energy (blue), vdW interaction energy (orange) and elastic deformation energy (dark cyan) between graphene and MoS_2 calculated for a2 × b2 (10.21 nm × 5.89 nm). The peak force site is at $z = 3.96$ Å.

$$= \sqrt{3}\left(\frac{\Delta\gamma\sigma_0^2}{2D}\right)^{1/4}\left(\frac{z}{\sigma_0}-1\right). \tag{29}$$

To verify the accuracy of our theory, we compared the simulated results with the theoretical values, as shown in Fig. 9. Obviously, the linear approximation of $\tan\theta_m$ is very close to our MD simulation results especially in the initial peeling stage.

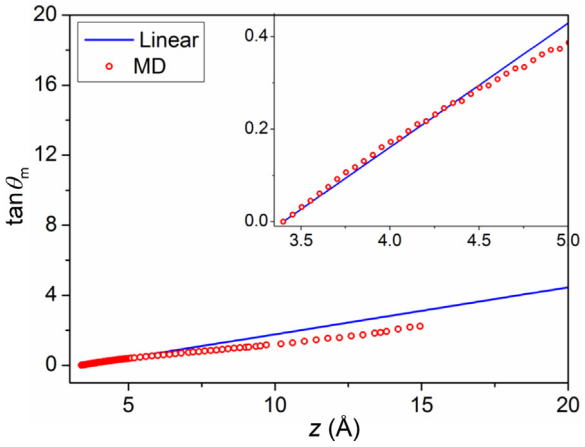

Fig. 9. Variations in the slope with changing peeling distance. Red circles are the MD simulation results; Blue is the linear approximation from Eq. (29). Insert is the local magnification.

Hence, we can substitute Eq. (29) into Eq. (19) to obtain the expression of the dimensionless peeling force

$$\frac{F}{F_0}=\frac{b\left[\left(\frac{\sigma_0}{z}\right)^{12}-2\left(\frac{\sigma_0}{z}\right)^{6}+1\right]\sqrt{1+3\left(\frac{\Delta\gamma\sigma_0^2}{2D}\right)^{1/2}\left(\frac{z}{\sigma_0}-1\right)^2}}{\sqrt{3}\left(\frac{\Delta\gamma\sigma_0^2}{2D}\right)^{1/4}\left(\frac{z}{\sigma_0}-1\right)}, \tag{30}$$

where b is a dimensionless width. We compared our theory with MD simulation results as shown in Fig. 10(a) and (b). In addition, a bending rigidity for graphene of 1.40 eV has been obtained by previous simulation [47]. The other parameters are obtained in the previous sections. It can be seen from the results that our theory can describe the peeling force perfectly, including during the initial stage, and the peak peeling force can be predicted accurately. In addition, the value of $\sin\theta_m$ approaches 1 as z increases. Hence, Eq. (30) is degenerate to the classical theory equation (15).

For peeling under a vertical force and bending moment loadings, the boundary conditions are symmetric in the quasi-state case, as shown in Fig. 7(f). Therefore, we can replace z in Eq. (29) with $(z+\sigma_0)/2$ to obtain the force:

$$\frac{F}{F_0}=\frac{b\left[\left(\frac{\sigma_0}{z}\right)^{12}-2\left(\frac{\sigma_0}{z}\right)^{6}+1\right]\sqrt{1+\frac{3}{4}\left(\frac{\Delta\gamma\sigma_0^2}{2D}\right)^{1/2}\left(\frac{z}{\sigma_0}-1\right)^2}}{\frac{\sqrt{3}}{2}\left(\frac{\Delta\gamma\sigma_0^2}{2D}\right)^{1/4}\left(\frac{z}{\sigma_0}-1\right)}. \tag{31}$$

Likewise, we compared our theory with MD simulation results as seen in Fig. 10(c) and (d). Our theory can be seen to describe the entire peeling process well. Hence, our theory can predict the force for peeling by adhesion.

3.5. Characteristic length and the theory expressed by the Hamaker constant

In the vertical peeling process, we found that the projection length $L(x)$ approaches a characteristic length, named the elasto-peeling length L_{ep}. When z increases, the tangential angle at the tip of the film approaches 90° ($\sin\theta\to 1$) and the force is equal to $\Delta\gamma b$; from Eq. (23), we can obtain:

$$L_{ep}=\sqrt{\frac{D}{\Delta\gamma/2}}. \tag{32}$$

Hence, in this case, the elasto-peeling length L_{ep} is approximately 1.83 nm, which perfectly matches the simulation results 1.74 nm. This characteristic length is physically significant: $\Delta\gamma$ is the work of adhesion, which is the surface energy of the two surfaces produced by peeling, and D is the bending rigidity of graphene. Hence, L_{ep} reflects the bending and interfacial properties of the layered materials during peeling. See Supplementary Fig. 1, the larger the bending rigidity or the smaller the work of adhesion, the larger the elasto-peeling length is. In addition, it

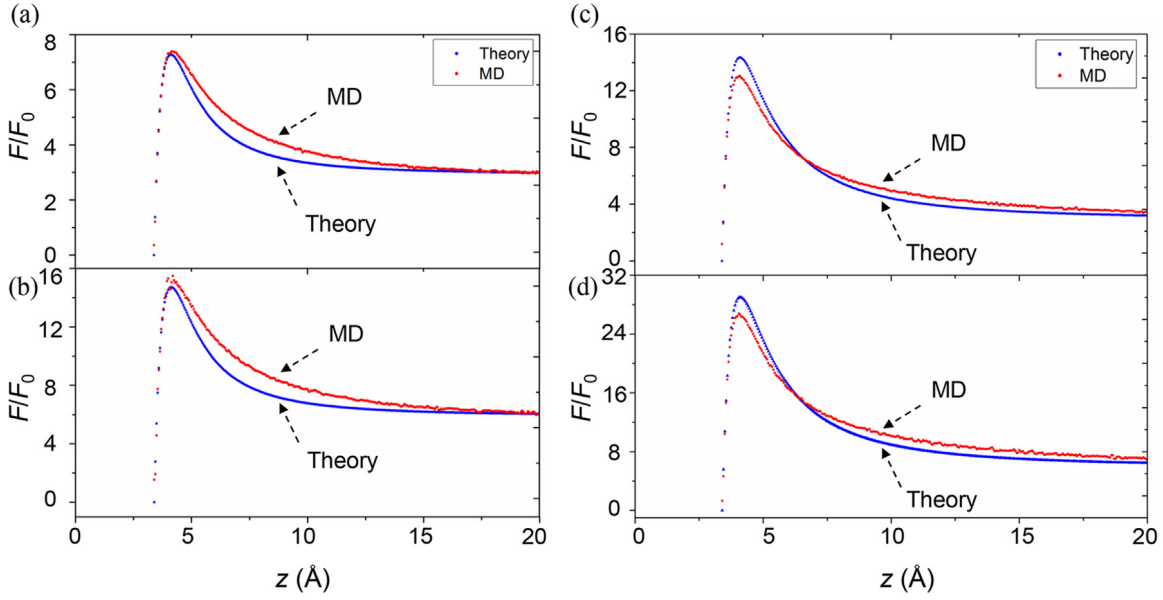

Fig. 10. Evolution of the dimensionless force. Red represents the MD simulation results, and blue represents the theory results. (a) A width of b1 = 2.91 nm and (b) a width of b2 = 5.89 nm are under vertical force loading. (c) A width of b1 = 2.91 nm and (d) a width of b2 = 5.89 nm are under vertical force and bending moment loadings.

has a certain similarity to the elastocapillary length [48–50]. With this elasto-peeling length, the peeling force from Eq. (30) can be transformed into:

$$\frac{F}{F_0}=\frac{b\left[\left(\frac{\sigma_0}{z}\right)^{12}-2\left(\frac{\sigma_0}{z}\right)^{6}+1\right]\sqrt{1+\frac{3\sigma_0}{L_{ep}}\left(\frac{z}{\sigma_0}-1\right)^2}}{\left(\frac{3\sigma_0}{L_{ep}}\right)^{1/2}\left(\frac{z}{\sigma_0}-1\right)}. \tag{33}$$

The evolutions of the dimensionless force for different elasto-peeling lengths are shown in Supplementary Fig. 2. The peak peeling force gradually approaches the stable peeling force as the elasto-peeling length decreases. Additionally, as the elasto-peeling length becomes larger, the initial peeling stage becomes longer.

To make the results as general as possible, the Hamaker constant $H=4\pi\varepsilon_{12}\rho_1\rho_2\sigma_{12}^6$ can be used to express the theory. The interaction potential energy per unit area between two homogeneous materials with atomic number densities ρ_1 and ρ_2 can be obtained by integration (see Supplementary Note 3 for details):

$$U_{12}=\frac{\pi\varepsilon_{12}\rho_1\rho_2}{3}\left(\frac{\sigma_{12}^{12}}{30r^8}-\frac{\sigma_{12}^6}{r^2}\right), \tag{34}$$

where σ_{12} and ε_{12} are potential parameters, and r is the distance between the two surfaces. Hence, we have

$$\begin{cases}\dfrac{\mathrm{d}U_{12}}{\mathrm{d}r}=0\Rightarrow r_0=\left(\dfrac{2}{15}\right)^{1/6}\sigma_{12}\\ U_{\min}=U_{12}\left(r_0\right)\Rightarrow U_{\min}=\dfrac{H}{16\pi r_0^2}.\end{cases} \tag{35}$$

In our model, the equilibrium distance is $\sigma_0=2^{1/6}\sigma_1$ and the corresponding potential energy is $\varepsilon\rho$. According to Eqs. (30) and (35), the force expressed by the Hamaker constant is

$$\frac{F}{F_0}=\frac{b\left[\left(\frac{\sigma_0}{z}\right)^{12}-2\left(\frac{\sigma_0}{z}\right)^{6}+1\right]\sqrt{1+\frac{3}{4}\left(\frac{H}{2\pi D}\right)^{1/2}\left(\frac{z}{\sigma_0}-1\right)^2}}{\frac{\sqrt{3}}{2}\left(\frac{H}{2\pi D}\right)^{1/4}\left(\frac{z}{\sigma_0}-1\right)}. \tag{36}$$

Additionally, $F_0=\Delta\gamma=H/16\pi\sigma_0^2$ is the peeling force for a 1 nm wide film. Then the elasto-peeling length can be expressed by Hamaker constant as follows:

$$L_{ep}=4\sigma_0\sqrt{\frac{2\pi D}{H}}, \tag{37}$$

it also has a certain similarity to the persistence length [51,52].

The interlayer interaction potential is adopted as the LJ 12-6 potential. If we adopt either the LJ 10-4 potential or the LJ 9-3 potential, we need to change the potential energy term. The premise being that both of these potential energies can describe the potential energy near the equilibrium position and for regions away from the equilibrium position, as shown in Fig. 2(d). Supposing a potential function of $G\left(\sigma_0,z\right)$:

$$\begin{aligned}\Gamma\left(H,D,\sigma_0,z\right)&=\frac{\sqrt{1+\frac{3}{4}\left(\frac{H}{2\pi D}\right)^{1/2}\left(\frac{z}{\sigma_0}-1\right)^2}}{\frac{\sqrt{3}}{2}\left(\frac{H}{2\pi D}\right)^{1/4}\left(\frac{z}{\sigma_0}-1\right)}\ \text{or}\\ \Gamma\left(L_{ep},\sigma_0,z\right)&=\frac{\sqrt{1+\frac{3\sigma_0}{L_{ep}}\left(\frac{z}{\sigma_0}-1\right)^2}}{\left(\frac{3\sigma_0}{L_{ep}}\right)^{1/2}\left(\frac{z}{\sigma_0}-1\right)},\end{aligned} \tag{38}$$

thus, the peeling force can be summarized as:

$$F=\begin{cases}b\Delta\gamma\left[G\left(\sigma_0,z\right)+1\right]\Gamma\left(L_{ep},\sigma_0,z\right) & \text{loading } F\\ b\Delta\gamma\left[G\left(\sigma_0,z\right)+1\right]\Gamma\left[L_{ep},\sigma_0,\left(z+\sigma_0\right)/2\right] & \\ \quad\text{loadings } F \text{ and } M & \\ b\Delta\gamma\quad G\to 0 \text{ and } \Gamma\to 1. & \end{cases} \tag{39}$$

Hence, if we obtain the equilibrium distance, the Hamaker constant or the work of adhesion between two films (they are interdependent parameters), the bending rigidity of the peeled film and the peeling width we can predict the evolution of the peeling force.

4. Conclusions

In summary, by DFT-D2 calculations, the final optimized lattice parameters of graphene and MoS_2 are 2.489 Å for graphene and 3.112 Å for MoS_2; the optimum distance between the monolayer of MoS_2 (S atom) and graphene is 3.31 ± 0.02 Å, and the binding energy is −22.1 meV per C atom. Additionally, we calculated the lattice mismatch as well as the intrinsic strain energy of the graphene/MoS_2 heterostructure caused by the lattice mismatch. In addition, the potential parameters for LJ 10-4, LJ 9-3 and LJ 12-6 were obtained. Then, MD simulations were performed to investigate the peeling process under two different loading conditions. We clarified the evolutions of the total energy, vdW interaction energy and elastic energy of graphene. By calculating the peeling force, we found there to be three stages in the entire peeling process, and the traditional model is only suitable for the stable stage. Moreover, there is a peak in the peeling force during the initial stage whose force is several times greater than the stable peeling force. Hence, we cannot ignore an accurate description of the initial stage, which drives us to explore the underlying mechanisms.

Consequently, mechanical models for the two different loading methods are established to investigate the peeling processes. Based on a quasi-continuum method, we have developed a new theory that can describe the entire process from initial contact to the stable peeling stage. In addition, we have obtained a new characteristic length, the elasto-peeling length $L_{ep}=\sqrt{2D/\Delta\gamma}=4\sigma_0\sqrt{2\pi D/H}$, that is a crucial parameter that reflects the bending and interfacial properties of the layered materials during peeling. Generally, this theory can be expressed by the Hamaker constant. We only need to know four physical quantities for the layered materials in the heterostructure to evaluate the evolution of the peeling force, which are the interlayer spacing σ_0, the work of adhesion between the layers $\Delta\gamma$ (or the Hamaker constant H), the bending rigidity D (or the elasto-peeling length L_{ep}) and the width d of the peeled layer. Our findings may help to understand the underlying mechanisms in the peeling of layered materials at the atomic scale and assist future mechanical assemblies of vdW heterostructures.

Acknowledgments

This research is supported in part by the National Natural Science Foundation of China (NSFC, Grant No. 51861145314 and 11872363), and by the Chinese Academy of Sciences (CAS) through CAS Interdisciplinary Innovation Team Project, the CAS Key Research Program of Frontier Sciences (Grant No. QYZDJ-SSW-JSC019) and the CAS Strategic Priority Research Program (Grant No. XDB22040401).

Appendix A. Supplementary data

Supplementary material related to this article can be found online at https://doi.org/10.1016/j.eml.2019.100501.

References

[1] K.S. Novoselov, A.K. Geim, S.V. Morozov, D. Jiang, Y. Zhang, S.V. Dubonos, I.V. Grigorieva, A.A. Firsov, Electric field effect in atomically thin carbon films, Science 306 (5696) (2004) 666–669.

[2] K.S. Novoselov, D. Jiang, F. Schedin, T.J. Booth, V.V. Khotkevich, S.V. Morozov, A.K. Geim, Two-dimensional atomic crystals, Proc. Natl. Acad. Sci. USA 102 (30) (2005) 10451–10453.

[3] K.F. Mak, C. Lee, J. Hone, J. Shan, T.F. Heinz, Atomically thin MoS_2: A new direct-gap semiconductor, Phys. Rev. Lett. 105 (13) (2010) 136805.

[4] M. Yankowitz, J. Xue, D. Cormode, J.D. Sanchez-Yamagishi, K. Watanabe, T. Taniguchi, P. Jarillo-Herrero, P. Jacquod, B.J. LeRoy, Emergence of superlattice Dirac points in graphene on hexagonal boron nitride, Nat. Phys. 8 (2012) 382.

[5] K.S. Novoselov, A. Mishchenko, A. Carvalho, A.H. Castro Neto, 2D materials and van der Waals heterostructures, Science 353 (6298) (2016) aac9439.

[6] A.K. Geim, I.V. Grigorieva, Van der Waals heterostructures, Nature 499 (2013) 419.

[7] H. Yang, J. Heo, S. Park, H.J. Song, D.H. Seo, K.-E. Byun, P. Kim, I. Yoo, H.-J. Chung, K. Kim, Graphene barristor, a triode device with a gate-controlled Schottky barrier, Science 336 (6085) (2012) 1140–1143.

[8] D. Jariwala, V.K. Sangwan, C.-C. Wu, P.L. Prabhumirashi, M.L. Geier, T.J. Marks, L.J. Lauhon, M.C. Hersam, Gate-tunable carbon nanotube–MoS_2 heterojunction pn diode, Proc. Natl. Acad. Sci. 110 (45) (2013) 18076–18080.

[9] D. Sarkar, X. Xie, W. Liu, W. Cao, J. Kang, Y. Gong, S. Kraemer, P.M. Ajayan, K. Banerjee, A subthermionic tunnel field-effect transistor with an atomically thin channel, Nature 526 (7571) (2015) 91–95.

[10] G. Konstantatos, M. Badioli, L. Gaudreau, J. Osmond, M. Bernechea, F.P.G. De Arquer, F. Gatti, F.H. Koppens, Hybrid graphene-quantum dot phototransistors with ultrahigh gain, Nat. Nanotechnol. 7 (6) (2012) 363–368.

[11] X. Gan, R.-J. Shiue, Y. Gao, I. Meric, T.F. Heinz, K. Shepard, J. Hone, S. Assefa, D. Englund, Chip-integrated ultrafast graphene photodetector with high responsivity, Nat. Photonics 7 (11) (2013) 883–887.

[12] O. Lopez-Sanchez, E. Alarcon Llado, V. Koman, A. Fontcuberta i Morral, A. Radenovic, A. Kis, Light generation and harvesting in a van der Waals heterostructure, Acs Nano 8 (3) (2014) 3042–3048.

[13] Y. Kobayashi, K. Kumakura, T. Akasaka, T. Makimoto, Layered boron nitride as a release layer for mechanical transfer of GaN-based devices, Nature 484 (7393) (2012) 223–227.

[14] N. Han, T.V. Cuong, M. Han, B.D. Ryu, S. Chandramohan, J.B. Park, J.H. Kang, Y.-J. Park, K.B. Ko, H.Y. Kim, Improved heat dissipation in gallium nitride light-emitting diodes with embedded graphene oxide pattern, Nature Commun. 4 (2013) 1452.

[15] E. Shi, H. Li, L. Yang, L. Zhang, Z. Li, P. Li, Y. Shang, S. Wu, X. Li, J. Wei, Colloidal antireflection coating improves graphene–silicon solar cells, Nano Lett. 13 (4) (2013) 1776–1781.

[16] M.-L. Tsai, S.-H. Su, J.-K. Chang, D.-S. Tsai, C.-H. Chen, C.-I. Wu, L.-J. Li, L.-J. Chen, J.-H. He, Monolayer MoS_2 heterojunction solar cells, ACS Nano 8 (8) (2014) 8317–8322.

[17] D. Jariwala, S.L. Howell, K.-S. Chen, J. Kang, V.K. Sangwan, S.A. Filippone, R. Turrisi, T.J. Marks, L.J. Lauhon, M.C. Hersam, Hybrid, gate-tunable, van der Waals p–n heterojunctions from pentacene and MoS_2, Nano Lett. 16 (1) (2015) 497–503.

[18] C.R. Woods, L. Britnell, A. Eckmann, R.S. Ma, J.C. Lu, H.M. Guo, X. Lin, G.L. Yu, Y. Cao, R.V. Gorbachev, A.V. Kretinin, J. Park, L.A. Ponomarenko, M.I. Katsnelson, Y.N. Gornostyrev, K. Watanabe, T. Taniguchi, C. Casiraghi, H.J. Gao, A.K. Geim, K.S. Novoselov, Commensurate–incommensurate transition in graphene on hexagonal boron nitride, Nat. Phys. 10 (2014) 451.

[19] C.H. Lui, Z. Ye, C. Ji, K.-C. Chiu, C.-T. Chou, T.I. Andersen, C. Means-Shively, H. Anderson, J.-M. Wu, T. Kidd, Y.-H. Lee, R. He, Observation of interlayer phonon modes in van der Waals heterostructures, Phys. Rev. B 91 (16) (2015) 165403.

[20] V. Birman, Control of fracture at the interface of dissimilar materials using randomly oriented inclusions and networks, Int. J. Eng. Sci. 130 (2018) 157–174.

[21] L. Li, M. Zhao, Structures, energetics, and electronic properties of multifarious stacking patterns for high-buckled and low-buckled silicene on the MoS_2 substrate, J. Phys. Chem. C 118 (33) (2014) 19129–19138.

[22] J.A. Robinson, Growing vertical in the flatland, ACS Nano 10 (1) (2016) 42–45.

[23] J.A. Miwa, M. Dendzik, S.S. Grønborg, M. Bianchi, J.V. Lauritsen, P. Hofmann, S. Ulstrup, Van der waals epitaxy of two-dimensional MoS2–graphene heterostructures in ultrahigh vacuum, ACS Nano 9 (6) (2015) 6502–6510.

[24] L. Yu, Y.-H. Lee, X. Ling, E.J.G. Santos, Y.C. Shin, Y. Lin, M. Dubey, E. Kaxiras, J. Kong, H. Wang, T. Palacios, Graphene/MoS_2Hybrid Technology for Large-Scale Two-Dimensional Electronics, Nano Lett. 14 (6) (2014) 3055–3063.

[25] A. Yan, J. Velasco, S. Kahn, K. Watanabe, T. Taniguchi, F. Wang, M.F. Crommie, A. Zettl, Direct growth of single- and few-layer MoS_2 on h-BN with preferred relative rotation angles, Nano Lett. 15 (10) (2015) 6324–6331.

[26] M. Cattelan, B. Markman, G. Lucchini, P.K. Das, I. Vobornik, J.A. Robinson, S. Agnoli, G. Granozzi, New strategy for the growth of complex heterostructures based on different 2D materials, Chem. Mater. 27 (11) (2015) 4105–4113.

[27] C.R. Dean, A.F. Young, I. Meric, C. Lee, L. Wang, S. Sorgenfrei, K. Watanabe, T. Taniguchi, P. Kim, K.L. Shepard, J. Hone, Boron nitride substrates for high-quality graphene electronics, Nat. Nanotechnol. 5 (2010) 722.

[28] J.N. Coleman, M. Lotya, A. O'Neill, S.D. Bergin, P.J. King, U. Khan, K. Young, A. Gaucher, S. De, R.J. Smith, I.V. Shvets, S.K. Arora, G. Stanton, H.-Y. Kim, K. Lee, G.T. Kim, G.S. Duesberg, T. Hallam, J.J. Boland, J.J. Wang, J.F. Donegan, J.C. Grunlan, G. Moriarty, A. Shmeliov, R.J. Nicholls, J.M. Perkins, E.M. Grieveson, K. Theuwissen, D.W. McComb, P.D. Nellist, V. Nicolosi, Two-dimensional nanosheets produced by liquid exfoliation of layered materials, Science 331 (6017) (2011) 568–571.

[29] V. Nicolosi, M. Chhowalla, M.G. Kanatzidis, M.S. Strano, J.N. Coleman, Liquid exfoliation of layered materials, Science 340 (6139) (2013) 1226419.

[30] Y. Zhang, Q. Liu, B. Xu, Liquid-assisted, etching-free, mechanical peeling of 2D materials, Extreme Mech. Lett. 16 (2017) 33–40.

[31] V.B. Shenoy, R. Miller, E.B. Tadmor, R. Phillips, M. Ortiz, Quasicontinuum models of interfacial structure and deformation, Phys. Rev. Lett. 80 (4) (1998) 742–745.

[32] Y.-P. Zhao, Nano and Mesoscopic Mechanics, Science Press, Beijing, 2014.

[33] G. Kresse, J. Furthmüller, Efficient iterative schemes for ab initio total-energy calculations using a plane-wave basis set, Phys. Rev. B 54 (16) (1996) 11169.

[34] G. Kresse, J. Furthmüller, Efficiency of ab-initio total energy calculations for metals and semiconductors using a plane-wave basis set, Comput. Mater. Sci. 6 (1) (1996) 15–50.

[35] S. Grimme, Semiempirical GGA-type density functional constructed with a long-range dispersion correction, J. Comput. Chem. 27 (15) (2006) 1787–1799.

[36] T. Bučko, J. Hafner, S. Lebègue, J.G. Ángyán, Improved description of the structure of molecular and layered crystals: Ab initio DFT calculations with van der Waals corrections, J. Phys. Chem. A 114 (43) (2010) 11814–11824.

[37] A. Ebnonnasir, B. Narayanan, S. Kodambaka, C.V. Ciobanu, Tunable MoS_2 bandgap in MoS_2-graphene heterostructures, Appl. Phys. Lett. 105 (3) (2014) 031603.

[38] S. Plimpton, Fast parallel algorithms for short-range molecular dynamics, J. Comput. Phys. 117 (1) (1995) 1–19.

[39] S.J. Stuart, A.B. Tutein, J.A. Harrison, A reactive potential for hydrocarbons with intermolecular interactions, J. Chem. Phys 112 (14) (2000) 6472–6486.

[40] J.-W. Jiang, J. Lan, J.-S. Wang, B. Li, Isotopic effects on the thermal conductivity of graphene nanoribbons: Localization mechanism, J. Appl. Phys. 107 (5) (2010) 054314.

[41] Q.-X. Pei, Y.-W. Zhang, Z.-D. Sha, V.B. Shenoy, Carbon isotope doping induced interfacial thermal resistance and thermal rectification in graphene, Appl. Phys. Lett. 100 (10) (2012) 101901.

[42] J.L. Ericksen, On the Cauchy-Born rule, Math. Mech. Solids 13 (3–4) (2008) 199–220.

[43] Y. Ma, Y. Dai, M. Guo, C. Niu, B. Huang, Graphene adhesion on MoS_2 monolayer: An ab initio study, Nanoscale 3 (9) (2011) 3883–3887.

[44] S. Li, C. Guangde, Y. Honggang, W. Yelong, N. Haibo, Z. Youzhang, Electronic properties of MoS_2 sandwiched between graphene monolayers, Europhys. Lett. 106 (4) (2014) 47003.

[45] R.S. Rivlin, The Effective Work of Adhesion, Springer New York, New York, 1997.

[46] K. Kendall, The adhesion and surface energy of elastic solids, J. Phys. D: Appl. Phys. 4 (8) (1971) 1186.

[47] L. Qiang, A. Marino, H. Rui, Elastic bending modulus of monolayer graphene, J. Phys. D: Appl. Phys. 42 (10) (2009) 102002.

[48] Y.-P. Zhao, Physical Mechanics of Surfaces and Interfaces, Science Press, Beijing, 2012.

[49] Z. Wang, F.-C. Wang, Y.-P. Zhao, Tap dance of a water droplet, Proc. Roy. Soc. A 468 (2145) (2012) 2485–2495.

[50] Q. Liu, T. Ouchi, L. Jin, R. Hayward, Z. Suo, Elastocapillary crease, Phys. Rev. Lett. 122 (9) (2019) 098003.

[51] Y.-P. Zhao, Modern Continuum Mechanics, Science Press, Beijing, 2016.

[52] B. Tinland, A. Pluen, J. Sturm, G. Weill, Persistence length of single-stranded DNA, Macromolecules 30 (19) (1997) 5763–5765.